Three-dimensional fluid-structure interaction simulations of a yarn subjected to the main nozzle flow of an air-jet weaving loom using a Chimera technique

Abstract

In air jet weaving looms, the main nozzle pulls the yarn from the prewinder by means of a high velocity air flow. The flexible yarn is excited by the flow and exhibits high amplitude oscillations. The motion of the yarn is important for the reliability and the attainable speed of the insertion. Fluid-structure interaction simulations calculate the interaction between the air flow and the yarn motion and could provide additional insight into the yarn behaviour. However, the use of an arbitrary Lagrangian-Eulerian approach for the deforming fluid domain around a flexible yarn typically results in severe mesh degradation, vastly reducing the accuracy of the calculations or limiting the physical time that can be simulated. In this research, the feasibility of using a Chimera technique to simulate the motion of a yarn interacting with the air flow from a main nozzle was investigated. This methodology combines a fixed background grid with a moving component grid deforming along with the yarn. The component grid is, however, not constrained by the boundaries of the flow domain allowing for large deformations with limited mesh degradation. Two separate cases were investigated. In the first case, the yarn was considered to be clamped

at the main nozzle inlet. For the second case, the yarn was allowed to move axially as the main nozzle pulled it from a drum storage system.

Keywords

weft yarn, insertion, main nozzle, fluid-structure interaction, dynamic mesh, Chimera, overset

Introduction

Air jet weaving looms use high speed air flow to propel the yarn and can attain high insertion rates due to the limited amount of moving mechanical components. This makes them well suited for mass production of fabrics. However, the motion of the yarn is governed by its interaction with the air flow and is, therefore, harder to control.

To better understand the motion of the yarn one can resort to fluid-structure interaction (FSI) simulations that take into account the mutual influence of the air flow and the deforming yarn. However, the use of an arbitrary Lagrangian-Eulerian (ALE) approach to handle the deforming fluid domain around the yarn with a single deforming grid is not ideal as the large yarn deformations can lead to mesh degradation, affecting the accuracy of the results and/or limiting the physical time that can be simulated.

Several models and simulation methodologies aimed at modelling the behaviour of a yarn in an air flow have already been investigated. One of the first investigations was performed by Uno[1] who set up a model for the calculation of the yarn velocity launched by a single

main nozzle using an empirical model for the nozzle flow, a model for the yarn unwinding force, a friction coefficient associated to the yarn and the assumption that the yarn travels straight along the jet axis. Salama et al.[2] opted for a very similar approach for yarn insertion through a (slotted) tube. Adanur and Mohamed[3] also adopted these methods to calculate the yarn tension during yarn unwinding from drum and loop storage systems. Celik et al.[4] incorporated the flow from the relay nozzles into an analogous model by using time and place factors for the different forces acting on the yarn. Nosraty et al.[5] used the model from Adanur and Mohamed[3] as a basis for their model to analyse the influence of yarn count and air supply pressure on weft yarn tension. Szabó et al.[6] established a similar methodology for confusor guide systems. They described the air flow in the confusor guides by an empirical model.

By resorting to computational mechanics more detailed analysis can be performed and more complicated situations can be considered. As will be explained in the following lines, generally, the computational effort and complexity increase as the aspect ratio of a fibre/yarn is increased for cases with a similar flow and structural material. A thinner or longer structure (higher aspect ratio), typically, has more degrees of freedom and the relative motion of the 2 extremities is less constrained. On the one hand this increases the computational requirements for the structural solver. On the other hand, when considering two-way coupling, the increased range (and possibly speed) of structural motion can induce additional complications with the mesh deformation in the flow solver. For a clamped-free case the amplitude of motion tends to increase towards the tip and a longer, more flexible

structure is more susceptible to curl-up. A discussion on the effect of aspect ratio on fluidelastic instabilities of a clamped-free cylinder can be found in Païdoussis[7]. There it is also stated that for large aspect ratios flow-induced tension effects become more important than the flexural rigidity of the cylinder. Notable work on the flutter instability of such long flexible cylinders (clamped-free) in axial flow has been performed by De Langre et al.[8]. Some examples of research using computational mechanics for analyses of yarn/fibre motion are provided next. Tang and Advani[9] considered the motion of a long flexible fiber (aspect ratio = 96) in a simple shear flow by modelling the fiber as a chain of spheres using a one-way coupling, which means that the flow exerts forces on the yarn, but that the effect of the yarn's displacement on the flow is not considered. The motion of the fibre was treated as a constrained optimization problem. Zeng et al.[10] analysed the fiber (aspect ratio = 140) motion in the nozzle of an air-jet spinning machine using a 2-dimensional, 2-way fluid structure interaction model with a Lagrangian approach for the fiber, which includes flow forces affecting the yarn and yarn displacement affecting the flow. The flow was considered to be laminar and incompressible, boundary layers were neglected. A qualitative comparison of the results with experiments was performed based on high speed footage and reasonable agreement was found. Belforte et al.[11] used a 2-dimensional computational fluid dynamics (CFD) simulation to calculate the drag force on a nylon yarn in a main nozzle and compared different turbulence models. De Meulemeester, Githaiga et al.[12] established a 1-dimensional model to analyse the tension in the yarn during yarn braking. De Meulemeester, Puissant et al.[13] performed numerical calculations focussed on

the unwinding of a yarn from a drum by a main nozzle. The aerodynamic forces were obtained from experimentally determined friction coefficients and an assumed velocity profile within the main nozzle. Pei and Yu[14] analysed the behaviour of a fiber (aspect ratio equal to 1500) in the nozzle of a Murata vortex spinning machine. The simulations were performed on a 2-dimensional planar geometry. 2-way interaction was considered and the motion of the fiber was handled using a mesh adaptivity scheme to generate a new mesh if elements became too distorted. Battochio et al.[15] investigated the behaviour of long polymeric fibres (aspect ratio up to 200 000) in a uniform turbulent flow field using a 2-dimensional model with 1-way coupling. The fibre was represented by a chain of rigid rods and modelled using an articulated-body algorithm; forces on the fibre were obtained using Reynolds number dependent force coefficients. Kondora and Asendrych[16] simulated the motion of relatively short fibres (aspect ratio up to 80) in a fibre suspension flow for a papermachine headbox. They used a particle-level simulation technique with 1-way coupling (the motion of the fibres did not influence the flow). The flow was considered to be 2D. Results were compared to experiments based on probability density functions of fibre orientation. While qualitative agreement was found, there were still quantitative discrepancies. Jin et al.[17] also used an adaptive grid method for 4-node tetrahedral elements to simulate the motion of a flexible fiber (aspect ratio equal to 30), in 3D, under different constraint conditions in a low Reynolds number flow. The motion of the fiber was analysed but no comparison with experiments or theory was provided. Wu et al.[18] focussed on the yarn whipping behaviour at the exit of the main nozzle during the start-up stage of an air-

jet loom. They employed 2-dimensional planar, 2-way FSI simulations ignoring the viscous forces on the yarn. Only the section of the yarn protruding from the main nozzle was considered and an ALE technique was used to cope with the yarn motion. Thorough experimental comparison was however not possible due to the 3D nature of the problem. Osman, Malengier et al.[19] combined a 3-dimensional structural model with a 2-dimensional, axisymmetric flow model to simulate the motion of a yarn as it is launched by a main nozzle. The influence of the yarn on the flow was incorporated by the use of an immersed boundary method allowing the fluid grid to remain fixed. A cylinder (no shear) was added on the axis of the main nozzle to account for the flow obstruction. Forces on the yarn were obtained from local flow and yarn velocities and an empirically determined force coefficient. A good quantitative agreement with the experiments in terms of yarn speed was observed. The yarn shape was also compared qualitatively to those from experiments at several time instants. Later Osman, Delcour et al.[20] carried out 3-dimensional, 2-way FSI-simulations for a yarn fixed at the main nozzle inlet using an ALE approach. Experimental wave speeds and wavelengths, obtained by visual analysis of snapshots, were compared to those observed in the simulations. The physical time that could be simulated was, however, limited due to mesh degradation. Therefore, in the current research a new approach was adopted based on the Chimera (or overset) technique: instead of considering a single fluid grid which is deformed using an ALE approach, 2 fluid grids were considered namely a background grid (fixed) and a component grid (deforming). The component grid moved along with the yarn and was deformed using an ALE approach, but it was not

constrained by the flow boundaries such as the walls of the main nozzle. As a result, large deformations could be calculated without severe mesh degradation, allowing the simulated physical time to be extended compared to Osman, Delcour et al.[20]. Simulations were still restricted to smooth monofilament yarns to avoid complications in the structural modelling of the yarn and the influence of yarn hairiness on the air-yarn interaction. This new approach was also demonstrated for simulations in which the yarn was allowed to move axially. Such simulations are difficult to implement using a single deforming grid as the motion of the yarn would require the simultaneous use of mesh deformation, layering and sliding interfaces.

The Chimera (overset) technique was conceptualized in the 1980's by, amongst others, Benek, Steger and Dougherty[21]. The main idea was to simplify the mesh generation process for complex geometries by generating meshes for each component separately and then overlapping them with a background grid and possibly each other in the simulation. Additionally, the Chimera technique allows the possibility of using different solution techniques in different domains (Ishikawa et al.[22]), alternative ways of adaptive grid refinement (Matsuno, Yamakawa and Satofuka[23]), easier implementation of dynamic meshes (Xuefei, Yuan and Zhansen[24]) and correspondingly facilitation of FSI simulations with large structural displacements (Santo et al.[25]) . The Chimera method has been under continuous development, with NASA as one of the main contributors. Prominent examples of the use of the Chimera technique for simulations of complex geometries are NASA's simulations of the space shuttle launch system vehicle (Gomez and Ma[26]) and the space

launch system vehicle (Rogers, Dalle and Chan[27]). The Chimera technique has often been applied in the CFD study of high-lift devices (Rogers et al.[28], Liao, Cai and Tsai[29], Levesque, Pigeon and Deloze[30]) and, more recently, for windturbine simulations (Santo et al.[25], Yu and Kwon[31], Sayed et al.[32]). A study comparing the Chimera technique for several CFD software packages was recently conducted by Chandar and Boppana[33]. By now the Chimera technique has been used and validated on quite some cases, including cases involving supersonic flows and shocks (Ishikawa et al.[22], Matsuno, Yamakawa and Satofuka[23], Xuefei, Yuan and Zhansen[24] and Rogers, Dalle and Chan[27]), which are also present in the current research. To the authors' best knowledge, this is the first time a Chimera technique was used in an FSI-simulation of a yarn in a main nozzle and that a 3D, CFD-based, 2-way FSI-simulation was performed on a long, axially-moving, flexible yarn in a high-Reynolds flow. In the considered application (main nozzle of an air jet weaving loom) the flow becomes highly turbulent upon entering the nozzle. The turbulent nature of the flow affects the forces exerted by the flow on the yarn.

The results from the simulations with the yarn fixed at the yarn inlet (clamped-free) were compared to experimental data. The experimental setup is described first, followed by a description of the simulation setup. The setup for the simulations with the yarn fixed at the yarn inlet and that in which the yarn is allowed to move axially are treated separately. Subsequently, results for the clamped-free case are provided and discussed. This includes a mesh sensitivity study, a comparison to previous ALE simulations and an alternative

method of comparing the results to the experiments based on frequency analysis. Lastly, some results from the simulation with the axially moving yarn are provided.

Experimental setup

Experimental data for the case with the yarn clamped at the main nozzle inlet was obtained from the experiments performed during the research of Osman, Delcour et al.[20]. A description of the experimental setup is provided in this section for completeness.

Figure 1 shows a sketch of the setup constructed by Picanol NV. It consisted of a main nozzle with a glass acceleration tube containing a yarn, clamped at the yarn inlet. The motion of the yarn was recorded with a high-speed camera (Photron FASTCAM SA4) recording at a rate of 10 000 fps. To be able to observe the yarn in the footage, the camera had to be positioned sufficiently close to the nozzle. Consequently, it was not possible to record the entire yarn at once. By displacing the camera, footage of both the first and second half of the yarn were obtained but these do not correspond to the same experimental run. Do note that the yarn motion was only recorded in the vertical plane.

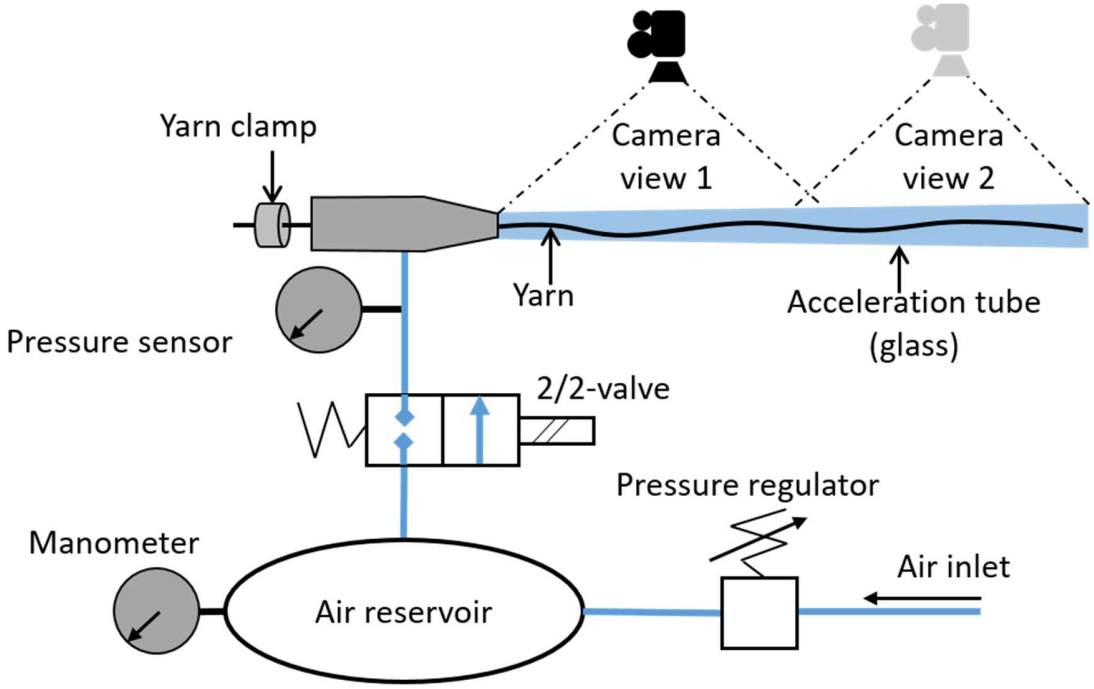

Figure 1: Sketch of the experimental setup with the yarn clamped at the main nozzle inlet.

Initially, the main nozzle was supplied with a holding flow pressure of 0.14 bar gauge. Afterwards, the supply pressure was increased to 5 bar gauge. With a supply pressure of 5 bar gauge the flow is choked at the throat section of the jet inlet. The subsequent expansion into the acceleration tube causes a region of supersonic flow, which through a series of oblique shocks becomes subsonic again. On average the air velocity inside the acceleration tube is about 300 m/s, corresponding to a Mach number of approximately 0.85. However, at the jet entrance, air velocities up to 560 m/s with a Mach number of 2.3 are reached. During the experiment the pressure at the nozzle inlet was measured using a piezo-resistive pressure transducer (Meggitt model 8530B, 200 psia range) sampling at a frequency of 10 kHz with a least count of 0.046 bar. The measured pressure profile is displayed in Figure 2.

This profile was used for specification of the inlet boundary condition in the flow simulation. The pressure at the inlet of the main nozzle (measured by the pressure sensor) showed some fluctuation. This was caused by pressure waves travelling in between the air reservoir and the main nozzle inlet.

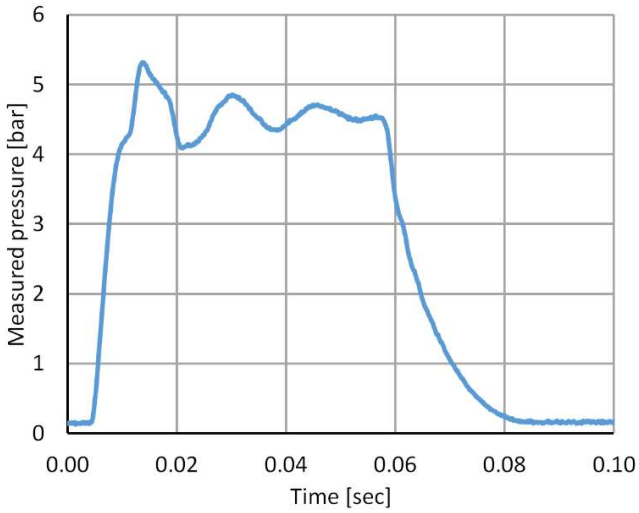

Figure 2. Measured pressure profile at the inlet of the main nozzle during the experiment. The values are relative to the atmospheric pressure.

Figure 3 shows a sketch of the nozzle geometry. For the experiment a monofilament nylon yarn was used with diameter 0.72 mm, a linear density of 464 tex (g/km) and a Young's modulus of 2.5 GPa.

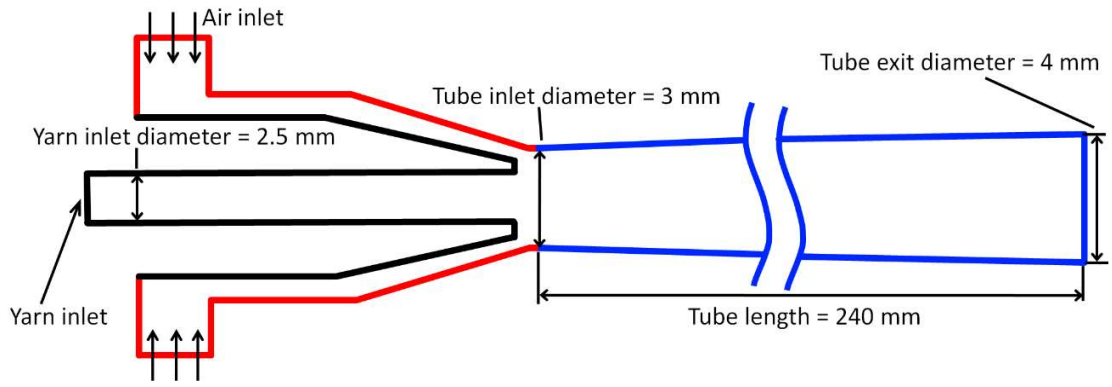

Figure 3. Meridional view of the geometry of the main nozzle. The red, black and blue lines represent the nozzle body, the needle and the tube, respectively.

Simulation setup

As mentioned in the introduction, a Chimera approach was opted for in this research to handle the yarn deformation in the flow calculation. This implies that meshes were superimposed in the flow solver and the solution was obtained by solving the flow equations on each grid using interpolated data from overlapping grids as boundary conditions to the solution. This methodology allows for a large flexibility in meshing and mesh motion but typically implies an increased computational cost. In the current research, two meshes were employed: a background mesh and a component mesh. The background mesh contained the entire flow domain and did not deform due to yarn motion. The component mesh corresponded to the flow in a cylindrical domain around the yarn. The component mesh moved and deformed along with the yarn, using an ALE-approach to obtain the solution on this grid.

Yarn clamped at the main nozzle inlet and free at the other end (clamped-free)

Flow Solver

For this case, with the yarn fixed at the main nozzle inlet, a sketch of the background mesh and its boundary conditions is provided in Figure 4 (a). Figure 4 (b) shows this for the component mesh. The meshes were superimposed so that, before deformation, the points A and B indicated on the component grid coincide with points A and B indicated on the background grid, respectively. An “overset interface” boundary condition is required to enable the Chimera technique and this boundary has to encapsulate the component mesh.

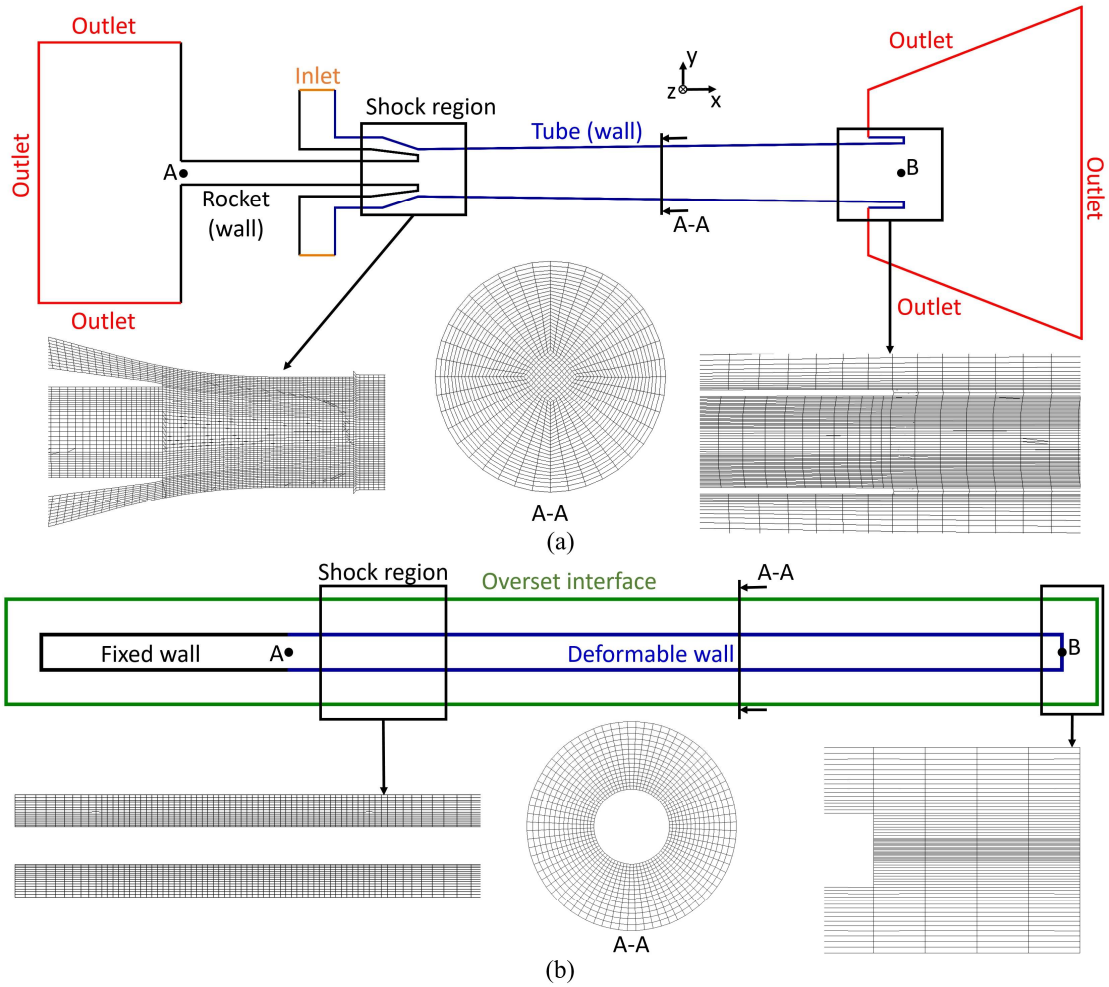

Figure 4. Meridional sections of the computational domain corresponding to (a) the background mesh and (b) the component mesh with indication of the boundary conditions for the clamped-free case. The grids are superimposed so that, without deformation, the points A and B from (a) overlap with those from (b). The yarn is clamped at point A.

The background and component mesh contained, respectively, 1.1 million and 275 000 hexahedral cells. In the circumferential direction 80 divisions were employed for both the component and the background mesh. The axial resolution on both grids was comparable and was increased towards the shock region and the exit of the acceleration tube. As is

mentioned in Xuefei, Yuan and Zhansen[24] it is important to have an adequate match between the grids in the shock region to maintain accuracy of the simulation. The background mesh was fixed, while the component mesh deformed along with the yarn as if it were a part of the yarn. For the mesh deformation of the component mesh a spring-based smoothing method without damping on the springs was used. This implies that the component mesh can be considered as a set of interconnected springs with an identical spring stiffness for all connecting edges. If damping of the springs would be enabled then edges further removed from the moving surface (yarn wall) would be less inclined to follow its motion and might introduce unwanted cell deformation. Damping of the springs is mainly intended for cases in which the outer boundary of the mesh or cells far removed from the moving surface should not deform too much. In this research, the overset interface was not constrained and it was intended to follow the yarn motion as closely as possible to maintain the original mesh quality. Therefore, no damping was applied and consequently, the overset interface followed all translational motions of the yarn. Rotational motions were followed up to a certain extent but resulted in some skewing of the cells.

Prior to actually solving the flow field a decision had to be made on what cells to use for interpolation of the solution between the grids. If desired the computational cost of Chimera calculations can be reduced by eliminating cells with overlap from the solution procedure; these cells are then referred to as “dead cells”. In the employed CFD software (ANSYS Fluent 18.2) this choice is made based on priority settings. For the calculations, under consideration the Chimera methodology was configured to maintain the integrity of the

component mesh as much as possible by assigning a higher grid priority to the component mesh.

The flow simulations were performed with the k-ω SST model. At the inlet the experimentally measured pressure profile (see Figure 2) was imposed as total pressure. The static pressure at the outlets (see Figure 4) was set to atmospheric pressure. All walls, including the yarn wall, were considered to be no-slip walls. A first-order implicit time stepping scheme was employed (as the second-order time stepping scheme is not yet compatible with the Chimera approach in ANSYS Fluent) with a time step size of 5e-6 seconds. The second-order upwind scheme was used for the convective terms in the density, momentum and energy equations to improve accuracy of the simulations.

Structural solver

The structural domain contained 2 components. The first component represented the yarn and consisted of 4800 elements of the type C3D20R (3D continuum elements with 20 nodes per elements and Reduced integration). The Young's modulus (E) was set to 2.5 GPa, the Poisson ratio (υ) to 0.39 and the linear density to 464 tex. The left end of the yarn was clamped (neither displacement nor rotation are allowed); the right end was free. The second component contained the structural model for the walls of the main nozzle.

The main nozzle walls were modelled by an analytical rigid body. It is a simplified representation of the actual nozzle geometry and was used solely for contact detection. Its radial dimension was reduced by 15% so that in the flow solver there was always some space in between the yarn wall and the nozzle wall. This is required as the Chimera method

needs a sufficiently large overlap region, as is for example mentioned in Levesque, Pigeon and Deloze[30]. The Chimera technique as implemented in ANSYS Fluent requires a minimum of 3 cells to be present in a gap. A 3D visualisation of the structural model, with a deformed yarn, is shown in Figure 5. The length of the yarn was 0.283 m. Structural simulations were performed in 3D with Abaqus 6.14 taking into account nonlinearity.

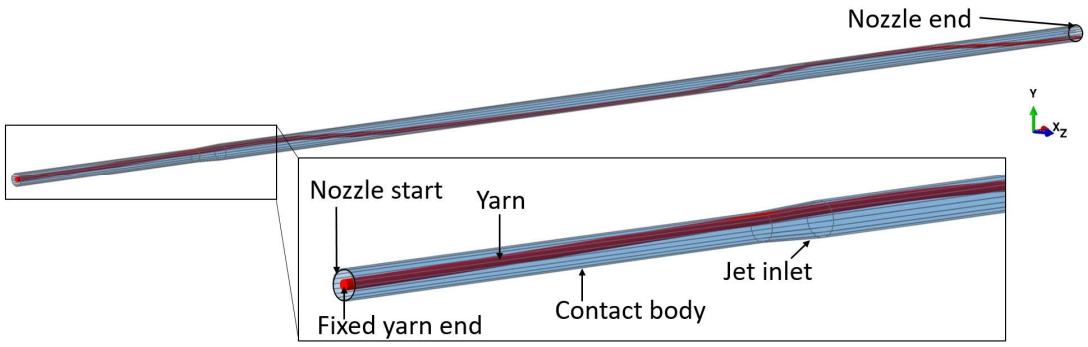

Figure 5: 3D visualization of the structural model for the clamped-free case.

The contact between the yarn and the nozzle wall was set as a frictionless contact in the tangential direction. The contact in the normal direction approximated a hard contact using a linear penalty method. A hard contact implies that no contact pressure is present unless the surfaces contact each other, that there is no limit to the magnitude of the contact pressure and that there is no penetration. In the current model some penetration was allowed due to the use of the linear penalty method. This method imposes a contact force proportional to the penetration distance. Furthermore, arbitrary motion was allowed between the contact surfaces and a surface-to-surface discretisation was used for the contact, which considers multiple nodes at once for contact conditions rather than each

node separately. The time step used in the structural solver was generally the same as for the flow solver (5e-6 s), however, under certain conditions (e.g. whipping of the yarn tip against the nozzle wall), a reduced structural time step was required to prevent divergence.

Axially moving yarn

In this setup the yarn was allowed to move axially and was considered to be pulled from a drum storage device. The setup is largely the same as for the clamped-free case. Important differences in the setup are highlighted in the following paragraphs.

Flow solver

The background mesh was the same as that used in the clamped-free case (Figure 4(a)) apart from the resolution in the circumferential direction. To save on computational time 40 instead of 80 circumferential cells were used for both the background and component mesh. The component mesh was again a cylinder encompassing the yarn. The yarn was now however 2 m long and was partly wound on a drum. Additionally, the axial resolution along the yarn was now uniform as every section of the yarn had to pass through the shock region, where the resolution of background grid and component grid should be comparable to maintain solution accuracy (in the clamped-free case a stretching could be applied reducing the total number of cells in the component grid). Figure 6 displays the background and component mesh. The background mesh now contains approximately 500 000 cells, the component mesh consists of 3.8 million cells.

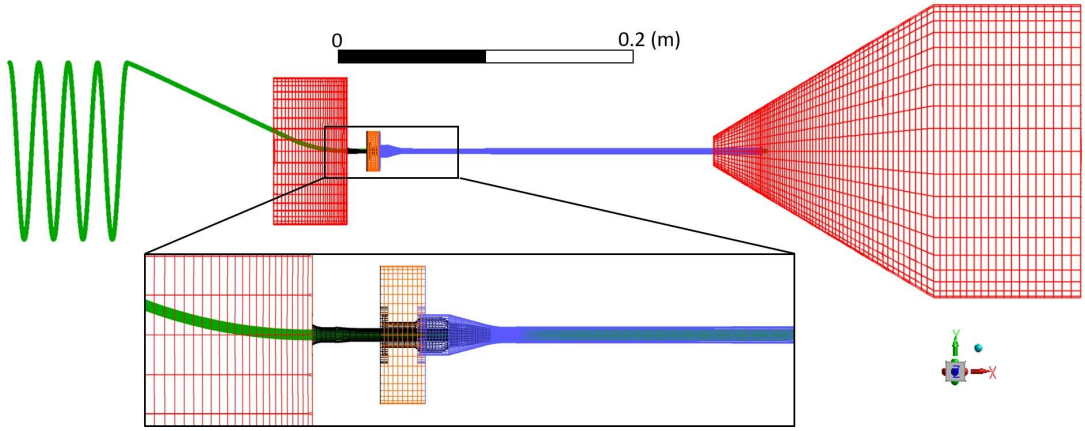

Figure 6: Mesh configuration used for the setup with axially moving yarn. Blue = tube (wall) ; Black = rocket (wall) ; Red = pressure outlets ; Orange = inlet; Green = overset interface (encompasses the component mesh).

As can be seen in Figure 6, a large part of the component mesh was located outside of the background mesh. During the calculation these cells are neglected by the flow solver until they enter the background mesh (due to axial motion). However, the structural solver still needed a certain load input for that section of the yarn. To do so the flow variables were considered to be frozen for cells located outside of the flow domain. The flow variables of component grid cells initially contained values assigned upon initialization. As long as the cells did not enter the background domain they retained these values. Upon entering the computational domain the values were updated based on the flow solution. Component grid cells exiting the computational domain retained the values they had prior to their exit. The force to be passed to the structural solver consisted of a pressure and a viscous force. The pressure force was easily obtained by multiplying the pressure in a wall adjacent cell with its corresponding area. The viscous force was obtained by relying on the law of the wall for which all required values are available in the cells. Remember that the values of

the flow variables remained frozen as long as the cells are outside of the computational domain. Nevertheless, the wall velocity, which followed from the mesh motion imposed by the structural solver, was updated and taken into account for the calculation of the wall shear stress. This approach relies on some approximations but allows for a reduction in computational cost due to a reduction in fluid cells. As long as the flow variables are more or less constant near the boundaries of the computational domain the approximation will have little influence.

In this setup, the yarn was free to move except at its starting point (leftmost end) where it was considered fixed. Initially, the same mesh deformation settings were used as for the clamped-free case. However, due to the yarn motion being less constrained, a larger twist on the yarn was possible which caused excessively skewed cells. To resolve this issue, the spring-based smoothing method was interchanged with a linearly elastic solid based smoothing method prior to the mesh becoming excessively distorted. The displacement of the internal nodes of the component mesh is then governed by the equilibrium stress-strain equations for a linear elastic solid with the imposed boundary motion acting as a boundary condition. To solve the equations a Poisson ratio had to be specified; in the current setup a value of 0.0 was opted for, implying that x, y and z deformations are decoupled. For example, a radial contraction of a cell will not yield an axial extension.

At the inlet again an experimentally measured pressure profile was imposed as total pressure. Compared to the clamped-free case the pressure now started immediately at a gauge pressure of about 4.7 bar and showed smaller fluctuations. The remainder of the

settings was the same as for the clamped-free case: this includes the boundary conditions at walls and outlets, time stepping scheme, time step size and discretization schemes.

Structural solver

Apart from the yarn being longer and partly wound on a drum (resulting in a spiral shape), the structural model did not differ much from that used for the clamped-free case. The structural model for the yarn now consisted of 65 000 elements of type C3D20R. The analytical rigid body for contact was prepended with a funnel to smoothly guide the yarn into the nozzle. Figure 7 visualises the structural model.

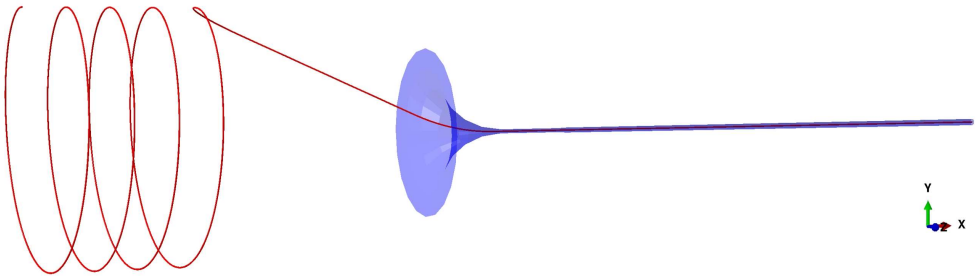

Figure 7: 3D visualization of the structural model for the axially moving yarn.

Coupling

The FSI calculations were performed using an in-house code named “Tango” which uses a partitioned approach. The coupling was implicit using the interface Quasi-Newton IQN-ILS technique (Degroote et al.[34]). A coupling iteration was considered to be converged when the vector norm of the matrix consisting of the displacement vector for each node in going from one coupling iteration to the next was smaller than 1e-6 m.

Results and Discussion

Clamped-Free yarn: Mesh sensitivity

To investigate the influence of mesh size, steady state calculations were performed for several mesh densities on the clamped-free case. For these calculations the pressure at the inlet was set to a total absolute pressure of 6 bar. The results are displayed in Figure 8.

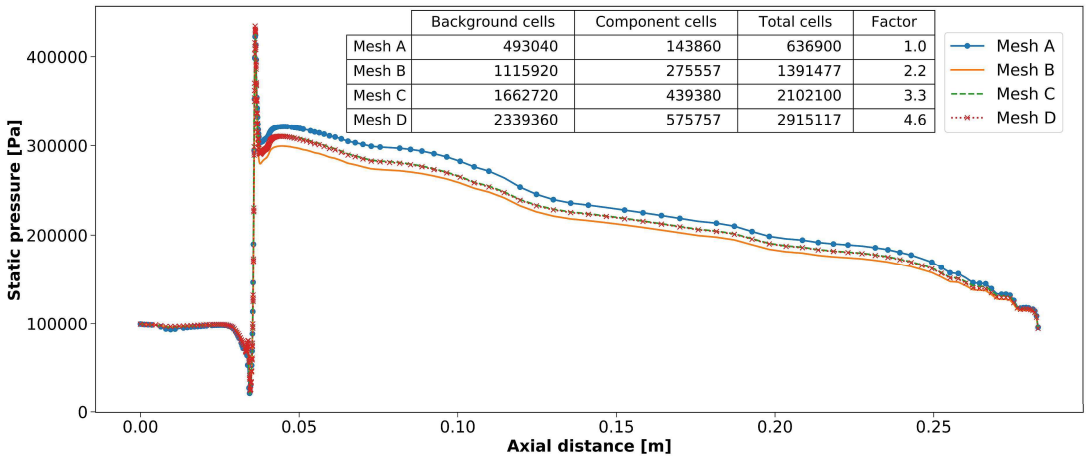

	Background cells	Component cells	Total cells	Factor
Mesh A	493040	143860	636900	1.0
Mesh B	1115920	275557	1391477	2.2
Mesh C	1662720	439380	2102100	3.3
Mesh D	2339360	575757	2915117	4.6

Figure 8: Circumferentially averaged static pressure along the yarn (located on the axis of the nozzle) for different mesh densities. The included table contains the number of cells in the background and component mesh. The column "total cells" contains the sum of both previous columns. The column "Factor" contains the ratio of the total number of cells in the current mesh to that of mesh A.

It can be observed that there is still some mesh dependence for Mesh A and B in Figure 8. Nevertheless, the main calculation has been performed on Mesh B to maintain a reasonable computational time. This mesh is already twice as fine as the one used in previous research (Osman, Delcour et al.[20]). In that research an increase in mesh density entailed a reduction in physical time that could be simulated due to more severe mesh degradation. The current

calculation was performed on mesh B over a longer time period, showing that the Chimera methodology allows for the use of finer meshes while also allowing for an extension of the simulated time.

Clamped-Free yarn: Comparison to ALE

Osman, Delcour et al.[20] performed simulations for a clamped-free yarn using an ALE approach. Results were compared to experiments on a quantitative and qualitative basis. The same quantitative comparison is repeated for the current simulations in which a Chimera technique is used.

Comparison is done based on the experimental footage of the first half of the yarn. For three waves the wavelength and wave speed are extracted from the footage. The simulated yarn motion is then examined over a similar time frame. Figure 9 displays the yarn position at 10 time instants in between 12.8 ms and 14.7 ms. The wavelength is defined as the distance in between 2 peaks within a single snaphot (points P and Q in the figure). If there are no 2 discernible peaks then the wavelength can also be estimated as 2 times the distance between a peak and the subsequent valley. The wave speed is determined by tracking a peak or valley as it travels along the yarn. In Figure 9 point P indicates the position of a peak at 12.8 ms. This peak is tracked and in the final frame (14.7 ms) it is located at point R. The distance between P and R divided by the time in between those snapshots yields the wave speed.

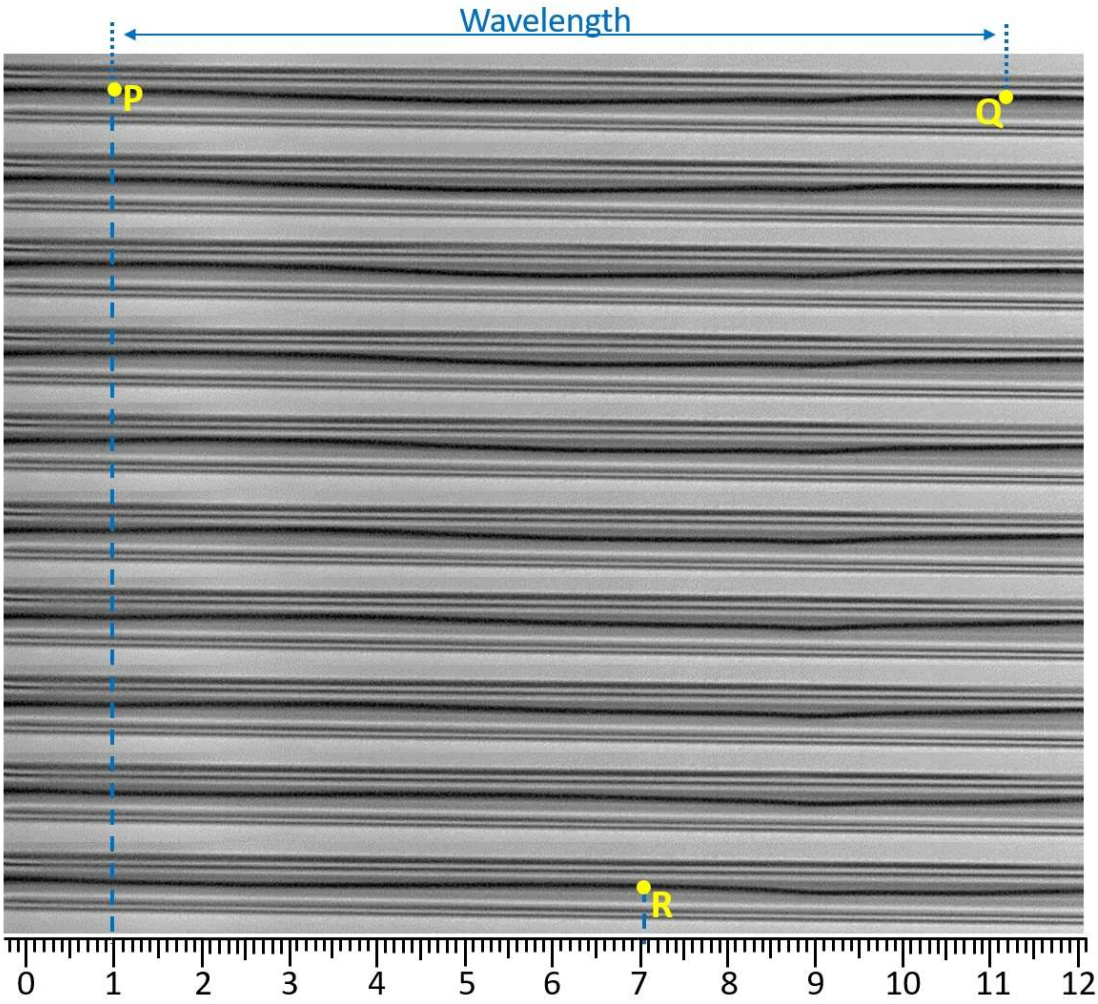

Figure 9: Snapshots of the the yarn in the first half of the tube at times 12.8, 13.0, 13.2, 13.4, 13.6, 13.8, 14.0, 14.2, 14.4 and 14.7 ms (top to bottom). Point P indicates the starting point of the peak that is tracked for determination of the wave speed; point R denotes its endpoint. Point Q indicates the location of the second peak in the first snapshot to define the wavelength.

To avoid a difference in mesh resolution with the previous work[20] the Chimera simulation considered is the one performed on the coarsest grid (See section "Mesh Sensitivity") in this section only. The exact time instants vary slightly as to more accurately observe the motion of crests and troughs. The comparison between the experiment, the ALE simulation

and the overset simulation is represented in Table 1. “Wave time” indicates the time interval over which the wave speed was determined.

Table 1: Comparison between experimental results, ALE (single grid) and Chimera calculation. C = wave speed, λ = wavelength, wave time = time interval over which wave speed was determined.

Experiment			ALE			Chimera		
Wave time [ms]	C [m/s]	λ [mm]	Wave time [ms]	C [m/s]	λ [mm]	Wave time [ms]	C [m/s]	λ [mm]
7.8 - 10.4	15.3	70	8.5 - 9.9	39.5	48	7.5 - 10.0	20.0	64
12.8 - 14.7	31.5	100	10.6 - 11.8	38.3	91	10.6 - 11.8	28.8	91
15.4 - 16.6	33.3	80	14.6 - 16.2	35.6	60	15.4 - 16.6	34.9	90

The table illustrates that the results obtained with the Chimera technique generally show a better correspondence with the experiments. This could result from the use of a dedicated component grid, a more accurately resolved boundary layer or the increased mesh quality (less mesh degradation).

To estimate the increase in computational cost the required computational time for the Chimera methodology was compared to that of the single-grid ALE approach. A series of 10 coupling iterations was performed on grids of similar resolution. The grid for the ALE method was composed out of 367 520 cells. The background grid for the Chimera method contained 493 040 (the volume of the yarn now also has to be meshed). The calculations were executed on 20 cores of a 2x12-core Intel Xeon E5-2680v3 2.5 GHz CPUs machine. For the ALE approach the flow solver ran for 848s, for the Chimera approach this was 941s, resulting in a factor of 1.2. It should also be mentioned that the reading and writing of files for the Chimera approach will require somewhat more time. The endured penalty will however depend largely on the data management plan and overall size of the case.

Using a single-grid ALE approach Osman, Delcour et al.[20] were able to simulate a total physical time of 17 ms. A grid of approximately 370 000 cells was used and refining the mesh resulted in more severe mesh degradation. In the current research a finer mesh (1.1M cells in the background grid) was used and the simulated time was doubled (34 ms). At the end of the simulation there is no sign of mesh degradation; after 6800 time steps the minimum orthogonal cell quality was 0.31, the same as at the start of the simulation. Based on these observations the simulation could be extended indefinitely. It should however be mentioned that at time step 3000 a local refinement was performed on the background mesh halfway the acceleration tube. This was required because initially the cells were stretched towards the centre of the tube. Upon maximum yarn deflection the misalignment between high aspect ratio component and background cells affected the quality of the interpolation. By refining the background mesh in that region the quality of the solution could be retained. Reaching time step 6800 required approximately 2 months of computational time on 60 cores. As the goal of the research was mainly to verify the feasibility of using a Chimera approach the calculations were not continued further in time.

Because the duration of the simulation could be extended, the comparison with experiments could also be performed at later times. Table 2 lists wavelengths and wave speeds for the first half of the yarn. Furthermore, at these later times, waves can also clearly be distinguished in the second half of the tube. This allows for a similar experimental comparison using footage from the second camera position (Table 3). The wave times were selected so that at the start and the finish of the interval, the peak/valley that was followed

was clearly discernible. Furthermore, the time interval had to be large enough to obtain an average wave velocity. It should be emphasized that the data in Table 2 and 3 were obtained from separate experiments. The camera had to be placed sufficiently close to the nozzle to be able to observe the vertical motion of the yarn. Therefore, only half the yarn could be visualised at once. Table 2 contains data of an experiment with the camera focussed on the first half of the yarn. Table 3 contains data of another experiment with the camera focussed on the second half of the yarn. Consequently, the wave times in both tables do not necessarily correspond. Overall, Table 2 contains data at earlier times as disturbances tend to develop close to the jet inlet and it takes some time for these to reach the second half of the tube.

Table 2: Comparison of Chimera technique (with 1.1M cells in the background grid) to experimental data of the first half of the yarn. C = wave speed, λ = wavelength, wave time = time interval over which wave speed was determined.

Experiment			Chimera		
Wave time [ms]	C [m/s]	λ [mm]	Wave time [ms]	C [m/s]	λ [mm]
7.8 - 10.4	15.3	70	7.5 - 10.0	20.0	69
12.8 - 14.7	31.5	100	12.8 - 14.7	33.0	118
15.4 - 16.6	33.3	80	15.4 - 16.6	34.9	93
26.5 - 27.9	32.1	82	27.5 - 28.5	33.0	87
29.0 - 30.2	37.0	80	29.0 - 30.0	37.8	84

Table 3: Comparison of Chimera technique (with 1.1M cells in the background grid) to experimental data of the second half of the yarn. C = wave speed, λ = wavelength, wave time = time interval over which wave speed was determined.

Experiment			Chimera		
Wave time [ms]	C [m/s]	λ [mm]	Wave time [ms]	C [m/s]	λ [mm]
20.9 - 22.4	31.3	88	20.5 - 21.5	29.2	78
26.5 - 27.7	35.0	102	26.0 - 27.0	40.6	95
31.0 - 32.2	44.2	114	31.0 - 32.0	44.7	96

The results as such generally show a relatively good agreement. It should, however, be mentioned that analysis of the footage only gives a rough estimate of the wave length and speed. Obtaining a wave length from the footage requires the localization of two extrema in a single snapshot, but the small radial dimensions of the tube make it difficult for clear wave shapes to develop. The extraction of wave speed from the footage is somewhat more robust as one can follow a certain peak or valley.

Figure 10 shows the simulated centreline position of the yarn at several time instants projected on the vertical plane. The inlet pressure is also plotted. Each dot on the pressure plot corresponds to the centreline position with the same color. The dashed lines denote the contact body; for visualisation purposes the radius of the contact body was reduced by 0.36 mm (the radius of the yarn). Contact between the plotted centreline and the plotted contact body then corresponds to contact between the yarn wall and the real contact body. The figure shows that as the valve is opened and the pressure at the nozzle inlet rises, a perturbation originates close to the jet inlet. This was also observed in the experimental

footage. The perturbation then moves along the yarn and eventually causes the yarn tip to violently whip against the nozzle wall.

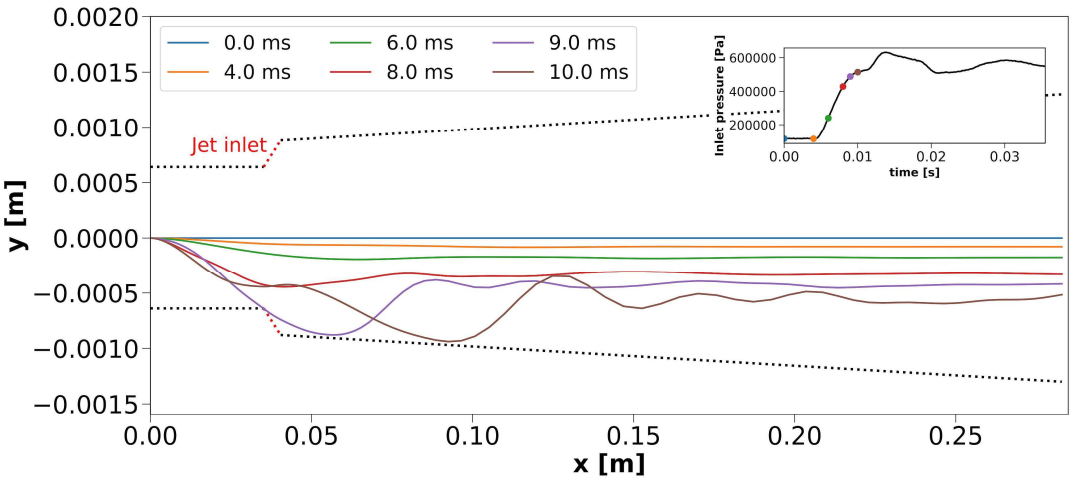

Figure 10: Centreline position as obtained from the simulation at several time instants. The inlet pressure is also plotted. Each dot on the pressure plot corresponds to a centreline position, plotted with the same color.

The simulations further showed that, after a while, the yarn tip tends to stick to the wall and move in a circulatory pattern. In a 2D projection this appears as an up-and-down motion of the tip, which was also seen in the experimental footage but that can, nevertheless, not fully confirm the circulatory motion.

Clamped-free yarn: Frequency analysis

As mentioned in the previous section, extracting wavelength and wave speed visually from the footage results in a rather rough estimate and can involve some subjectivity. Because the simulation could now be extended in time, a more objective comparison can be sought for. Due to the additional simulated time a more quasi-periodic behaviour could develop

and a certain point on the yarn is subjected to more passing waves. Figure 11 displays the motion of a point at 80% of the tube length projected on the vertical plane. It can be observed that after an initial transient the vertical displacement displays a quasi-periodic behaviour (in between the dashed lines). A frequency analysis of the vertical motion of this point can be compared to a frequency analysis of a point at the same location in the experiments. The amplitude of the vertical motion is limited by local contact with the wall of the acceleration tube. This is hinted at in Figure 11 by the consistency in the maximal and minimal vertical displacement. It should be mentioned that the diameter of the acceleration tube gradually increases from 3 mm at its start to 4 mm at its end. Therefore, the amplitude of the motion also tends to increase towards the nozzle end. Do note that due to simulation restrictions the contact body's radial dimensions are 15% smaller than in reality.

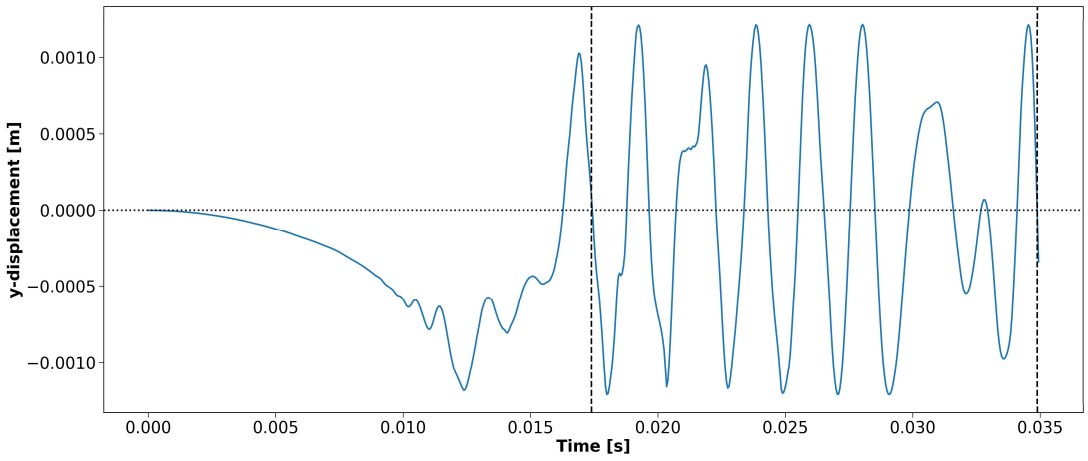

Figure 11: Vertical displacement of a point at 80% of the tube length as obtained from the simulation. Dashed vertical lines indicate the time interval used for the Fourier decomposition presented in Figure 14.

A snapshot from the experiment can be postprocessed to yield a result as depicted in Figure 12. Applying this to every frame and focussing on a point at a certain axial distance yields a result as shown in Figure 13.

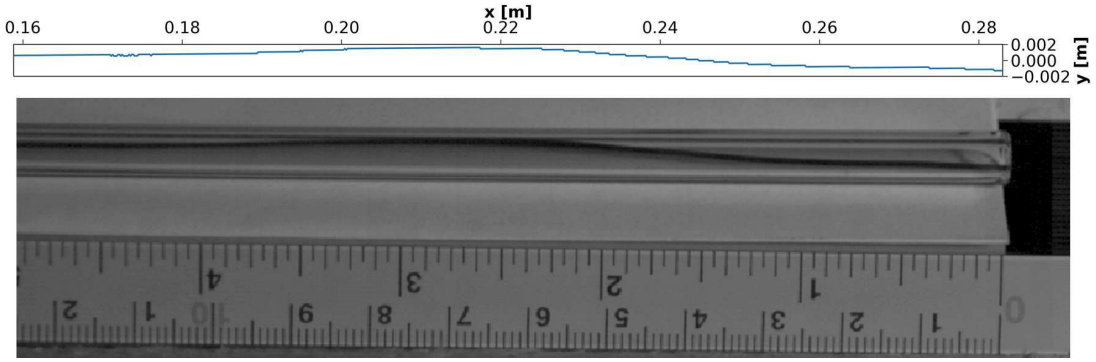

Figure 12: Example of a postprocessed snapshot (time = 43.2 ms) with the camera at position 2. Bottom: Image as retrieved from the camera. Top: Postprocessed result.

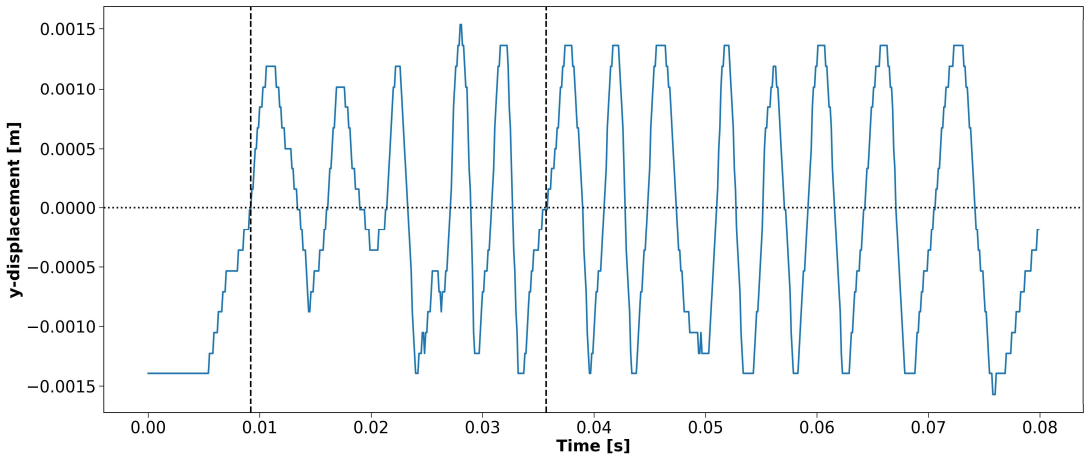

Figure 13: Vertical displacement of a point at 80% of the tube length as obtained from the experimental footage. Dashed vertical lines indicate the time interval used for the Fourier decomposition presented in Figure 14.

The vertical dashed lines in Figure 11 and 13 indicate approximately the same time interval. Applying a discrete Fourier transform to the data within those intervals yields the result represented in Figure 14.

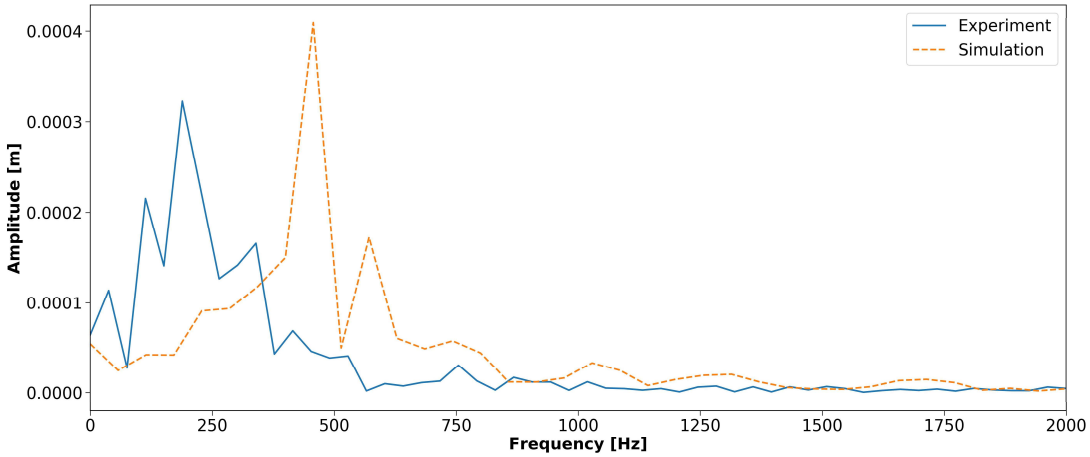

Figure 14: Discrete Fourier transform applied to the vertical motion of a point located 80% into the tube. The considered time intervals are indicated on Figures 11 (Simulation) and 13 (Experiment).

From Figure 14 it is clear that for the considered point the dominant frequency in the simulations is approximately twice that observed in the experiment, indicating that some fine tuning of the simulations might be required. For example, the diameter of the contact body in the simulations is smaller than in reality. Changing this diameter to better approximate the reality could increase the correspondence with experiments as will be explained later on.

As was mentioned previously, the yarn tip tends to stay in contact with the tube wall and move in a circulatory pattern according to the simulations. In fact when analysing the 3D motion of the yarn in the simulation the entire yarn appears to develop a swirling motion. Therefore a similar circulatory motion can be observed at other locations along the yarn. Figure 15 displays the y- and z-motion of a point 20% into the acceleration tube.

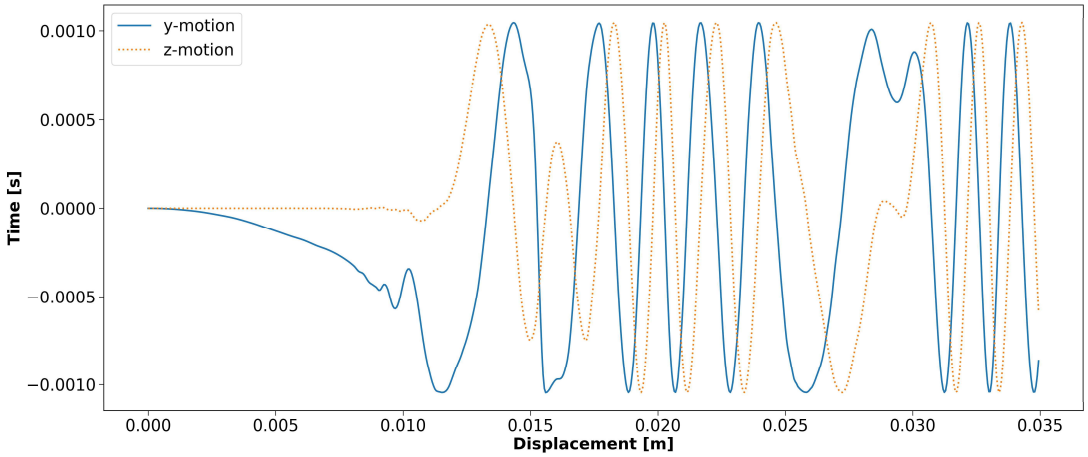

Figure 15: y- and z-motion of a point 20% into the acceleration tube in the simulation. The phase difference between both is indicative of a dominant circulatory motion.

It can be seen that the z-motion corresponds quite well to the y-motion but with a small phase difference, indicating a circulatory motion. The amplitude of the total displacement indicates that the yarn contacts the tube. Because during a substantial part of the simulation a large part of the yarn moves against the tube wall it was hypothesised that maybe the friction between the yarn and tube wall should be taken into account. Part of the simulation was therefore repeated with friction between the tube wall and the yarn. The friction coefficient was chosen rather high to make any difference clearly observable ($\mu = 1.0 + 0.4\ e^{-v}$; v being the relative velocity of both walls). Nevertheless only a negligible influence was observed.

Another, more prominent, difference between simulation and experiment is the radial dimension of the contact body. In the simulations the radial size of the contact body was reduced so that in the fluid solver there would always be sufficient space in between the yarn and the tube wall. In single grid approaches, this is required to ensure sufficient mesh

quality as otherwise cells get squeezed into a very small region and reach very high aspect ratios. For the Chimera technique, this space is required since the solver needs to be able to find donor and receptor cells in the gap for the interpolation between the background and component mesh. The Chimera technique as implemented in Fluent requires a minimum of 3 cells to be present in the gap. This implies that with a higher wall resolution one can get closer to the wall. To be able to compare with the previous single-grid ALE approach the same reduction of the radial dimension was employed for the Chimera simulation.

Increasing the radial dimensions of the contact body requires an increase of the near-wall resolution and, consequently, an increase in the number of cells. This would further increase the computational cost of the simulation. Therefore, such a simulation could not be performed at the moment.

From the footage and the simulations it can be deduced that waves tend to run along the yarn from jet inlet to acceleration tube outlet. Furthermore, the waves appear to be triggered by contact with the tube. Therefore, it is reasonable to assume that the wavelength is related to the size of the contact body. A smaller contact body is likely to result in a shorter wavelength. From the Euler-Bernouilli beam theory, the following formula for the wave speed (c) of travelling harmonic transversal waves as a function of their wavelength (λ) can be deduced:

$$c = \frac{2 \cdot \pi \cdot b}{\lambda} \tag{1}$$

$$\text{with } b^2 = \frac{EI}{\rho A} = 0.284^2 \quad (2)$$

with E the Young's modulus of the yarn, I the area moment of inertia, A its area and ρ the density of the yarn in kg/m³.

Previously, a wave speed was extracted from the footage by following a crest or a trough of the travelling wave as it moves along the yarn (See Figure 9 for an example).. Another possibility is to plot the displacement as a function of time for 2 points with a fixed distance in between (a distance of 20 mm was chosen) and then checking the time between a zero-crossing at point 1 and a zero crossing at point 2. By averaging this data for several passing waves a local wave velocity can be extracted for both simulation and experiment. Figure 16 illustrates the principle for the experiments at a distance of 80% into the tube. Sometimes due to for example harsh contact a disruptive wave can travel backwards and cause a "negative wavespeed" these datapoints should be excluded from the averaging as they cannot be related to the wavespeed of the forward travelling wave under consideration. Using this approach wave speeds are extracted for points at 20, 40, 60 and 80% of the tube; the results are listed in Table 4.

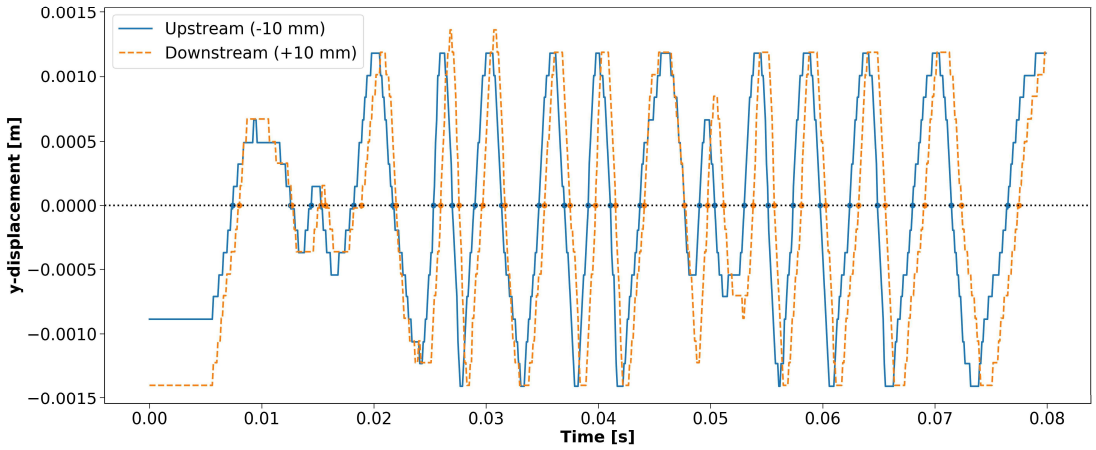

Figure 16: Vertical motion observed for 2 points 20 mm apart in the experiments. The points are centred around a location 80% into the tube.

Table 4: Wave speed extracted from the time in between two zero-crossings for points with 20 mm in between. These points are positioned 10 mm upstream and 10 mm downstream of the axial position mentioned in the first column. The percentage in the first column denotes the relative position in the acceleration tube [0% = start of acceleration tube, 100% = end of acceleration tube]. The final column indicates the ratio between the simulated and the experimental wave speed.

Axial position [%]	Experiment [m/s]	Simulation [m/s]	Ratio
20	42.63	48.53	1.138
40	35.54	45.77	1.288
60	35.44	44.31	1.250
80	35.50	48.63	1.370

In Table 4 the average ratio between the simulated and the experimental velocity is 1.26. Assuming formula (1) applies this would imply that the wavelengths in the experiment are 1.26 times larger than those from the simulation. For a travelling wave the frequency (f) of motion observed in a fixed point can be expressed as a function of the wave speed and wavelength.

$$f = \frac{c}{\lambda} \tag{3}$$

Substituting formula (1) into formula (3) indicates a quadratic dependence of the frequency on the wavelength:

$$f = \frac{2\pi b}{\lambda^2} \tag{4}$$

From graphs such as Figure 13 (for the experiment) and Figure 11 (for the simulation) one can select a time frame in which the motion is more or less periodic, by counting the number of periods in that interval an average frequency can be derived. This method was applied to points at 20, 40, 60 and 80% into the acceleration tube. The results are provided in Table 5. A corrected simulation frequency is obtained by dividing it with the previously obtained average ratio to the second power (1.26^2).

Table 5: Frequencies obtained from counting the number of periods of the vertical motion of points located 20, 40, 60 and 80% into the acceleration tube within a selected time interval. The corrected simulated frequency is obtained by dividing the simulated frequency by 1.26^2.

Axial position [%]	Experimental frequency [Hz]	Simulated frequency [Hz]	Corrected simulated frequency [Hz]
20	242	443	278
40	250	453	285
60	219	441	277
80	213	436	274

The correspondence between the experimental and the corrected simulated frequency is not yet perfect but shows decent agreement. This could imply that the radial dimension of the contact body can have a significant influence on the observed frequencies in the tube. It should also be mentioned that the manufacturing of a glass acceleration tube with an average diameter of 3.5 mm is not straightforward resulting in some uncertainty on the exact dimensions of the tube and therefore the experimental frequency.

Axially moving yarn

A big drawback of using a single-grid ALE approach is the difficulty involved in allowing for axial movement of the yarn. The basic mesh deformation algorithms do not alter the connectivity between nodes. Automatic remeshing is far from straightforward for structured meshes and resorting to unstructured meshes while maintaining the same simulation quality would vastly increase the computational cost. The use of sliding interfaces offers some additional motional freedom but still poses some limitations to the yarn motion.

The Chimera technique on the other hand poses very little limitations and the yarn motion can be transferred to the flow solver using basic mesh deformation algorithms. To illustrate the flexibility of the Chimera technique, a simulation was performed in which the yarn is considered to be stored on a drum (located outside of the flow domain) and was propelled by the main nozzle. For an illustration of the setup the reader is referred back to Figure 6. Figure 17 shows the yarn position in the simulation projected on the vertical plane at several time instants. The simulation was continued until the yarn tip reached the end of the flow domain. This implies that by the end of the simulation the yarn tip has progressed approximately 22 cm.

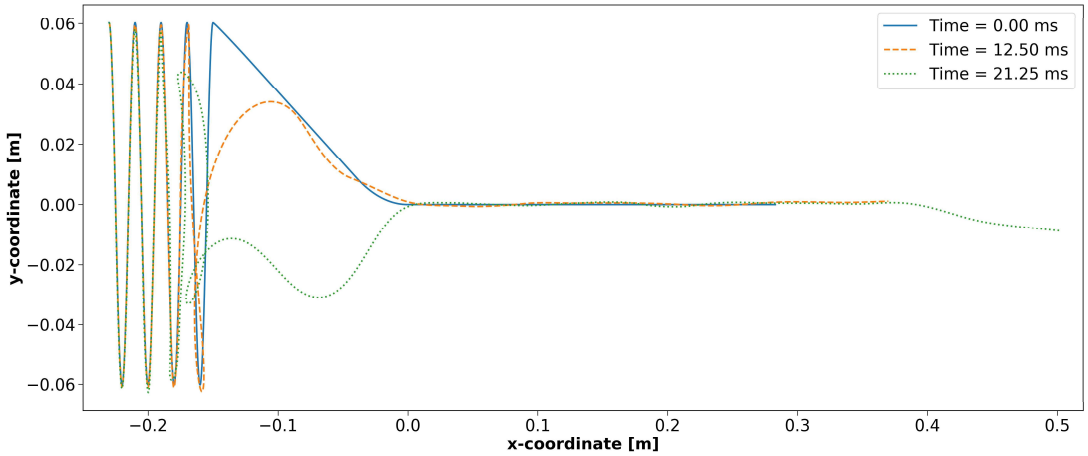

Figure 17: Position of the yarn centreline in the simulation projected on the vertical plane at several time instants.

In Figure 18, the axial velocity of the yarn tip as a function of time is plotted. The yarn tip initially displays a nearly constant acceleration. Towards the end of the simulation the tip velocity starts levelling out at approximately 16.2 m/s.

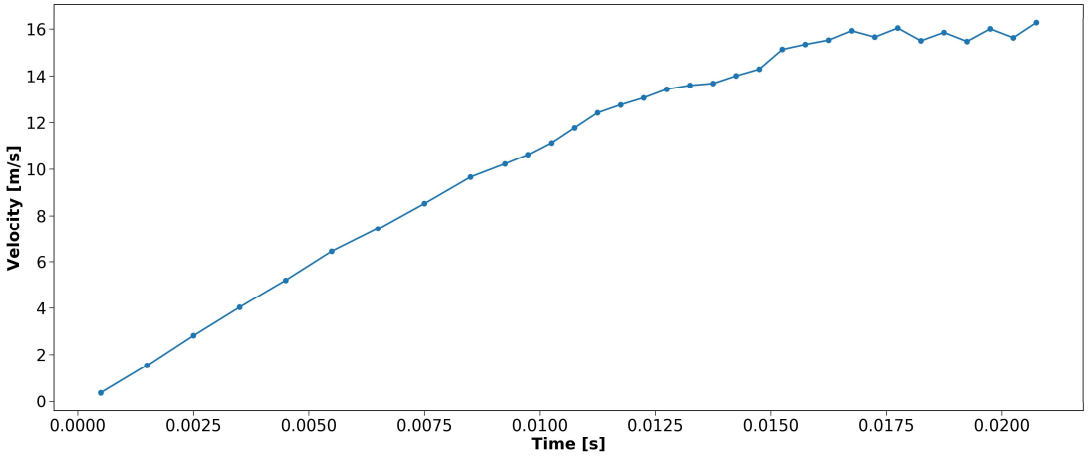

Figure 18: Simulated axial velocity of the yarn tip.

Conclusion

Attempts at simulating the motion of a clamped-free yarn inside the main nozzle of an air-jet weaving loom using a single deforming grid have shown difficulties dealing with the large yarn deformations due to mesh degradation, which become worse as the mesh is refined. This limits the physical time that can be simulated and as a consequence the possible validation with experiments. Additionally, one would like to be able to simulate the launch of a yarn, implying an axial motion which is hard to incorporate into the flow solver when using a single deforming grid.

By resorting to a Chimera technique, superimposing a fixed background grid and a component grid (that moves along with the yarn), both problems can be solved. First of all, the component mesh is not limited by the structure of the nozzle which allows for large deformations without substantial mesh degradation occurring. Consequently, finer meshes can be used if desired and the limitation on the physical time that can be simulated vanishes which allows for a more elaborate comparison with experimental data. Secondly, there is no strict mesh connectivity between the background and the component mesh. As a result the component mesh, including the yarn, can be made to move axially using simple mesh deformation algorithms. The Chimera technique has been in continuous development since the 1980's and has, by now, been applied and validated on numerous occasions including cases with supersonic flows and shocks. When dealing with shocks it is important to match mesh densities in their vicinity as well as possible to maintain accuracy.

For the case at hand the Chimera technique shows similar results as the single-grid ALE technique but the computational cost increases slightly. A more in-depth comparison with experiments showed that the results of the simulation for the clamped-free case still deviate substantially from the experimental data. Friction between the yarn and tube wall was shown not to be the cause. However, the reduction in radial dimension of the contact body might have a large influence on the simulated frequency.

When dealing with high aspect ratio cells on both grids in an overlapping region misalignment of component and background mesh can cause some inaccuracy and should be treated with care. In the flow solver contact between walls as a result of mesh motion should be avoided. A gap of at least 3 cells should be maintained between walls of component and background mesh. For the component mesh a spring-based mesh deformation algorithm could not accommodate all motions of the yarn. However, switching to a linear elastic solid based deformation algorithm has proven to be adequate in such cases.

Although the simulations still deviate from the experiments, the Chimera technique allows for large yarn deformations and axial motion to be incorporated into the flow solver at a slightly increased computational cost. Special care should be taken with regards to the mesh resolution in shock regions. When performing FSI simulations with the possibility of contact between bodies, measures should be taken to maintain sufficient space in between those walls. Better correspondence with the experiments might be attainable by further refining the mesh, resulting in a more accurate solution of the boundary layer on the yarn

while also allowing the contact body to be enlarged and better approximate the real nozzle wall. However, there is always a lot of uncertainty due to for example initial conditions, variations in structure along the yarn and deviations in nozzle dimensions.

References

1. Uno M. A Study on Air-Jet Loom with Substreams Added, Part 1: Deriving the equation of motion for weft. *J Textile Mach Soc Jpn* 1972; 25: 48-56.
2. Salama M, Adanur S and Mohamed MH. Mechanics of a Single Nozzle Air-Jet Filling Insertion System Part III: Yarn Insertion Through Tubes. *Text. Res. J.* 1987; 57: 44-54.
3. Adanur S and Mohamed MH. Analysis of yarn tension in air-jet filling insertion. *Text. Res. J.* 1991; 61: 259-266.
4. Celik N, Babaarslan O and Bandara MPU. A mathematical model for numerical simulation of weft insertion on air-jet weaving machine. *Text. Res. J.* 2004; 74: 236-240.
5. Nosraty H, Jedi AAA and Mousaloo Y. Simulation analysis of weft yarn motion in single nozzle air-jet loom to study the effective parameters. *Indian J. Fibre Text. Res* 2008; 33: 45-51.
6. Szabó L, Patkó I and Oroszlány G. The dynamic study of the weft insertion of air jet weaving machines. *Acta Polytechnica Hungarica* 2010; 7: 93-107.
7. Païdoussis MP. Fluid-Structure Interactions: Slender Structures and Axial Flow

(Volume 2). Kidlington, Oxford, U.K.: Academic Press; 2016.

8. De Langre E, Païdoussis MP, Doaré O and Modarres-Sadeghi Y. Flutter of long flexibly cylinders in axial flow. *Journal of fluid mechanics* 2007; 571: 371-389.
9. Tang W and Advani SG. Dynamic simulation of long flexible fibers in shear flow. *CMES* 2005; 8: 165-176.
10. Zeng YC, Yang JP and Yu CW. Mixed Euler-Lagrange approach to modeling fiber motion in high speed air flow. *Appl. Math. Modell.* 2005; 29: 253-261.
11. Belforte G, Mattiazzo G, Viktorov V, et al. Numerical Model of an Air-Jet Loom Main Nozzle for Drag Forces Evaluation. *Text. Res. J.* 2009; 79: 1664-1669.
12. De Meulemeester S, Githaiga J, Van Langenhove L, et al. Simulation of the dynamic yarn behavior on airjet looms. *Text. Res. J.* 2005; 75: 724-730.
13. De Meulemeester S, Puissant P and Van Langenhove L. Three-dimensional Simulation of the Dynamic Yarn Behavior on Air-jet Looms. *Text. Res. J.* 2009; 79: 1706-1714.
14. Pei Z and Yu C. Numerical study on the effect of nozzle pressure and yarn delivery speed on the fiber motion in the nozzle of Murata vortex spinning. *J. Fluids Struct.* 2011; 27: 121-133.
15. Battocchio F, Sutcliffe MPF and Teschner F. Dynamic simulation of long polymeric fibres immersed in a turbulent air flow. In: *Proceedings of the IMSD2012 - The 2nd Joint International Conference on Multibody System Dynamics*, Stuttgart, Germany, 29 May –1 June 2012, http://www2.eng.cam.ac.uk/~mpfs/papers/BST2012FibreTurbulentIMSD.pdf.

16. Kondora G and Asendrych D. Modelling of the dynamics of flexible and rigid fibres. *Chemical and Process Engineering* 2013; 34: 87-100.
17. Jin Y, Li J, Zhu L, et al. Three-dimensional Numerical Simulation of the Movement of the Flexible Body under Different Constraints. *J Therm Sci* 2014; 23: 593-599.
18. Wu Z, Chen S, Liu Y, et al. Air-flow characteristics and yarn whipping during start-up stage of air-jet weft insertion. *Text. Res. J.* 2016; 86: 1988-1999.
19. Osman A, Malengier B, De Meulemeester S, et al. Simulation of air flow-yarn interaction inside the main nozzle of an air jet loom. *Text. Res. J.* 2017; 88: 1173-1183.
20. Osman A, Delcour L, Hertens I, et al. Toward three-dimensional modeling of the interaction between the air flow and a clamped–free yarn inside the main nozzle of an air jet loom. *Text. Res. J.* Epub ahead of print 14 February 2018. DOI: 10.1177/ 0040517518758006.
21. Benek JA, Steger JL and Dougherty FC. A flexible grid embedding technique with application to the Euler equations. *6th Computational Fluid Dynamics Conference*, Danvers, MA, U.S.A., 13 July - 15 July 1983.
22. Ishikawa H, Tanaka K, Makino Y, Kazuomi Y. Sonic-boom prediction using Euler cfd codes with structured/unstructured overset method. *27th international congress of the aeronautical sciences*, Nice, France, 19 September - 24 September 2010.
23. Matsuno K, Yamakawa M, Satofuka N. Overset adaptive-grid method with applications to compressible flows. *Computers & Fluids* 1998; 27:599-610.
24. Xuefei L, Yuan L, Zhansen Q. Applications of overset grid technique to CFD

simulation of high mach number multi-body interaction/separation flow. *Procedia Engineering* 2015; 99:458-476.

25. Santo G, Peeters M, Van Paepegem W, Degroote J. Dynamic load and stress analysis of a large horizontal axis wind turbine using full scale fluid-structure interaction simulation. *Renewable energy* 2019; 140:212-226.
26. Gomez RJ, Ma EC. Validation of a large scale chimera grid system for the space shuttle launch vehicle. *12th Applied Aerodynamics Conference*, Colorado Springs, CO ,U.S.A., 20 June - 23 June 1994.
27. Rogers SE, Dalle DJ, Chan WM. CFD simulations of the space launch system ascent aerodynamics and booster separation. *53rd AIAA Aerospace Sciences Meeting*, Kissimee, Florida, U.S.A., 5 January - 9 January 2015.
28. Rogers SE, Roth K, Nash SM, Baker MD, Slotnick JP, Whitlock M, Cao HV. Advances in overset CFD processes applied to subsonic high-lift aircraft. *18th AIAA Applied Aerodynamics Conference,* Denver, Colorado, U.S.A., 14 August - 17 August 2014.
29. Liao W, Cai J, Tsai HM. A multigrid overset grid flow solver with implicit hole cutting method. *Computer methods in applied mechanics and engineering* 2007; 196:1701-1715.
30. Levesque AT, Pigeon A, Deloze T. An overset grid 2D/infinite swept wing URANS solver using recursive Cartesian virtual grid method. *53rd AIAA Aerospace Sciences Meeting*, Kissimee, Florida, U.S.A., 5 January - 9 January 2015.
31. Yu DO, Kwon OJ. Predicting wind turbine blade loads and aeroelastic response using

a coupled CFD-CSD method. *Renewable energy* 2014; 70:184-196.

32. Sayed M et al. High fidelity CFD-CSD aeroelastic analysis of slender bladed horizontal-axis wind turbine. *Journal of Physics: Conference series* 753 (2016) 042009.
33. Chandar DDJ, Boppana VBL. A comparative study of different overset grid solvers between OpenFOAM, STAR-CCM+ and ANSYS-Fluent. *2018 AIAA Aerospace Sciences Meeting, AIAA SciTech Forum,* Kissimee, Florida, U.S.A., 8 January - 12 January 2018.
34. Degroote J, Bathe KJ and Vierendeels J. Performance of a new partitioned procedure versus a monolithic procedure in fluid–structure interaction. *Comput Struct* 2009; 87: 793–801.